Prediction and Detection of Virtual Reality induced Cybersickness: A Spiking Neural Network Approach Using Spatiotemporal EEG Brain Data and Heart Rate Variability

1 **Prediction and Detection of VR induced Cybersickness: A Spiking Neural Network**

2 **Approach Using Spatiotemporal EEG Brain Data and Heart Rate Variability**

3

4 **Alexander Hui Xiang Yang[a], Nikola Kirilov Kasabov[b,c,g] and Yusuf Ozgur Cakmak[a,d,e,f*]**

5

6 a Department of Anatomy, University of Otago, Dunedin, New Zealand

7 b KEDRI, School of Engineering, Computing and Mathematical Sciences, Auckland

8 University of Technology, New Zealand

9 c George Moore Chair of Data Analytics, Ulster University, Londonderry, United Kingdom

10 d Medtech Core NZ, Auckland, New Zealand

11 e Brain Health Research Centre, Dunedin, New Zealand

12 f Centre for Health Systems and Technology, Dunedin, New Zealand

13 g Institute for Information & Communication Technologies, Bulgarian Academy of Sciences

14

15 **Correspondence:**

16 Yusuf Ozgur Cakmak

17 yusuf.cakmak@otago.ac.nz

21

22

23

24

25

26 **Abstract**

27 Virtual Reality (VR) allows users to interact with 3D immersive environments, and will be a

28 key technology across many domain applications, including access to a future metaverse.

29 Yet, consumer adoption of VR technology is limited by cybersickness (CS) - a debilitating

30 sensation accompanied by a cluster of symptoms including nausea, oculomotor issues and

31 dizziness. A leading problem is the lack of automated objective tools to predict or detect CS

32 in individuals, which can then be used for resistance training, timely warning systems or

33 clinical intervention. This paper explores the spatiotemporal brain dynamics and heart rate

34 variability involved in cybersickness, and uses this information to both predict and detect CS

35 episodes. The present study applies deep learning of EEG in a spiking neural network (SNN)

36 architecture to predict CS prior to using VR (85.9%, F7) and detect it (76.6%, FP1, Cz). ECG

37 derived sympathetic heart rate variability (HRV) parameters can be used for both prediction

38 (74.2%) and detection (72.6%) but at a lower accuracy than EEG. Multimodal data fusion of

39 EEG and sympathetic HRV does not change this accuracy compared to ECG alone. The

40 study found that Cz (premotor and supplementary motor cortex) and O2 (primary visual

41 cortex) are key hubs in functionally connected networks associated with both CS events and

42 susceptibility to CS. F7 is also suggested as a key area involved in integration of information

43 and implementation of responses to incongruent environments that induce cybersickness.

44 Consequently, Cz, O2 and F7 are presented here as promising targets for intervention.

45

46 **Keywords**: Cybersickness; Virtual reality, Spiking neural networks; EEG, ECG, NeuCube.

47

48

49

50

51

52

Introduction

Virtual Reality (VR) technology is becoming prevalent in entertainment, art, education, social and professional settings[1,2]. VR allows for interactive immersion into shared digital environments that can be accessed by many. Despite this, individual experiences in VR remain far from idyllic. Drawbacks exist in the form of cybersickness (CS) - a debilitating sensation accompanied by a cluster of symptoms that include nausea, oculomotor issues and dizziness[3]. It is unfortunate that limitations to human physiology and perception form a barrier to consumer adoption of VR technology; especially since our world continually charges towards a nexus of virtual and real-world interactions. A way to combat CS would be to utilize a tool that predicts or detects it. Yet, these tools must be automated and objective, so that preparations or active responses like training resistance, timely warning systems and clinical intervention can be implemented. Tracking of CS is currently restricted to subjective reports through verbal confirmation or questionnaires. Not only do these methods not allow for future prediction, but they are time inefficient and require manual input. With current technology at our disposal, objective biomarkers correlated with cybersickness can be collected from wearable devices and fed into machine learning algorithms for streamlined, automatic prediction and/or detection of cybersickness events[4]. While various models for prediction and detection of CS severity have been proposed[4,5], there lacks a way to both collect CS data and continue to generate new knowledge about the condition through machine learning assisted approaches. To achieve this, the present study uses a modified version of the brain-inspired NeuCube SNN architecture[6] to both predict and detect CS whilst generating new knowledge about the condition.

75

76

77   There are several reasons for choosing SNNs for this purpose. SNNs are advanced machine

78   learning techniques[7] and are considered the third generation of artificial neural networks.

79   They simulate the behaviour of biological neural networks by creating and updating

80   connections between spiking neurons (synaptic connections) to learn temporal associations

81   between them. This architecture and mechanism of learning has several advantages in

82   temporal information processing[8-13] over that of traditional neural networks. This includes

83   robustness to noise through the encoding of consecutive time series data, such as EEG, into a

84   compressed data format known as spikes (binary units) [7]. Encoding procedures such as

85   threshold-based-spike-generation, produce spikes that represent a change in consecutive

86   values above a certain threshold, allowing for changes in data to be captured over time .

87   Additionally, if multiple time series, such as EEG channels, are modelled in a single SNN,

88   patterns of interactions between the changes in their time series can be detected and analysed.

89   SNN architectures can further benefit from the usage of brain templates that specify a spatial

90   distribution in the anatomical shape of a brain. Upon training, these models can be considered

91   an interpretable spatiotemporal map of the brain activities measured, which assists to better

92   understand brain dynamics under diverse conditions. Further on, this spatiotemporal map can

93   be represented as a feature vector, and additional parameters from other biologically relevant

94   data such as HRV can be added for classification of different brain states.

95

96   Consequently, the present study performs deep learning of integrated EEG and sympathetic

97   heart rate variability (HRV) data in an interpretable dynamically evolving spiking neural

98   network (SNN) architecture. This architecture mimics the biological structure and processing

99   mechanisms of the human brain, and captures spatiotemporal information from EEG signals

100   to form a dynamically updateable neural map of CS. A machine learning algorithm was

101 developed that can detect CS events (76.6%) and predict it prior to VR usage at resting

102 baseline (85.9%) using electroencephalogram (EEG) data. F7 alone was the most optimal

103 input for cybersickness prediction. The algorithm also integrated fusion of electrocardiogram

104 (ECG) heart rate variability data but it did not improve classification accuracy. The study

105 found that features related to cybersickness susceptibility are diverse and that highlighted

106 features change over time. Amongst many important features, Cz (premotor and

107 supplementary motor cortex) and O2 (primary visual cortex) are key hubs in functionally

108 connected networks associated with both CS events and susceptibility to CS. According to

109 accuracy results and analysis of CS related brain hubs, Cz, O2 and F7 present as promising

110 targets for intervention. The study additionally proceeded with an exhaustive analysis to find

111 the best time segment during a resting-state EEG baseline and its data length for optimal

112 prediction accuracy.

113

114 **Contributions**

115 In summary, the paper contributes the following:

116 - A novel approach to the prediction and detection of cybersickness using interpretable

117 spiking neural networks (SNN) and weighted K-nearest neighbor (KNN) algorithms

118 using EEG and ECG data, both separately and in their integration.

119 - Optimized SNN architecture based on inherent characteristics of cybersickness

120 - Machine learning assisted knowledge discovery and insight into the spatiotemporal

121 brain dynamics of cybersickness

122 - Considerations for feature reduction for diagnostic and predictive CS computational

123 models.

124 - Machine learning extracted clinical biomarkers for the development of intervention

125 strategies.

126   -

127   **Methods**

128   *Subjects*

129   Sixty-four participants, male (29) and female (35), age range of 18-33 years (mean 23,

130   standard deviation ± 4.1). Subjects were recruited from the student and working population.

131   The exclusion criteria were a previous diagnosis of neurological disorder, cardiovascular

132   disease, diabetes, gastrointestinal disorder, medications, or smoking. All subjects had either

133   normal or corrected visual acuity with contact lenses. This study was approved by the

134   University of Otago Ethics Committee (H20/169) and performed in accordance with relevant

135   guidelines and regulations. All participants provided signed consent.

136

137   *Experimental equipment*

138   A VR video of rotating stars published by previous researchers was played in an HTC Vive

139   headset (HTC Corporation, Taipei, Taiwan). EEG was recorded using starstim32

140   (Neuroelectrics). ECG was recorded using Shimmer3 5 lead ECG (Shimmer, Dublin, Ireland)

141   at a sampling rate of 512 Hz. Five electrodes were placed, two 5 cm above the pelvic girdle,

142   labelled according to proximity towards the left leg (LL) and right leg (RL), and two 5 cm

143   below the clavicle, labelled according to proximity towards the left arm (LA) and right arm

144   (RA), with the fifth electrode at the V3 position relating to the midway point between the 4th

145   and 5th intercostal space. Data obtained from the LL-RA channel between electrodes was

146   used for analysis.

147
148   *Software*

149   iMotions 8.0 (iMotions, Cophenhagen, Denmark) was used to synchronize EEG and ECG

150   data recordings for a unified collection of measurement time series. Live view of biosensor

151   data streaming ensured quality data collection and so that markers separating baseline,

152   stimulation and post stimulation could be placed during the experiment. Neucube was used

153   for the SNN architecture and feature vector production. Python 3.8.8 was used for the

154   classification algorithms. HRV was analyzed using Kubios HRV Premium Ver. 3.3

155   software[14] (Kubios, Kuopio, Eastern Finland). For 10s HRV results, Neurokit2[15] was

156   used to determine R-peaks and pyHRV[16] was used to calculate RMSSD. The VR video

157   used in this experiment was developed in previous work by researchers from Stanford

158   University, and was chosen for its propensity to induce cybersickness in individuals. The VR

159   video consists of clockwise rotating white dots about the roll axis, dispersed at different

160   depths through the visual foreground and background[17].

161

162   *Protocol*

163   Participants (n=64) underwent a 2 minute resting state baseline (A) before VR immersion

164   without HMD usage, then watched a 2 minute VR video of rotating stars (B), followed by

165   removal of the headset and a 2 minute recovery period. EEG and ECG was recorded

166   continuously throughout the entire experiment. To mitigate any potential noise, participant

167   immersion in VR was a passive ordeal where the only requirement was to stare straight ahead

168   with minimal body and head movement, and all parts the experiment were seated. The

169   conscious perception of cybersickness was reported via a thumbs up, and was simultaneously

170   marked on the data stream. Individuals who reported cybersickness and those that did not

171   (controls) were separated into two groups. A pre-experiment motion sickness susceptibility

172   questionnaire[18] (MSSQ-Short) was administered to assess motion sickness history and

173   susceptibility, along with a post-experiment simulator sickness questionnaire[19] (SSQ) to

174   collect individual sickness ratings.

175
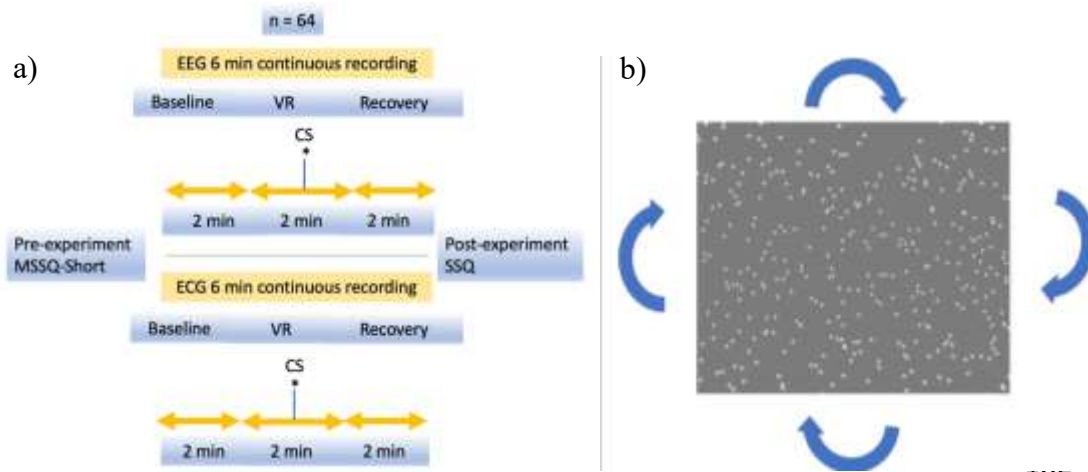
Figure 1. **a)** Experiment flow, **b)** VR video example

Statistics

A Mann-Whitney U test was run to compare between cybersick and control groups for the

following data: MSSQ-short scores, SSQ scores, spike count and HRV parameters -

Parasympathetic nervous system index (PNS), sympathetic nervous system index (SNS),

stress index (SI), standard deviation of N-N intervals (SDNN), root mean squared of

successive differences of R-R intervals (RMSSD).

The NeuCube brain-inspired Spiking Neural Network Architecture [18]

The following sections below describe the general architecture of the model and data pipeline.

This includes initial encoding of the raw EEG data into spikes, training of the SNN reservoir

for knowledge discovery and feature selection, producing a feature vector which represents the

spiking activity in the neural network through connections with an output neuron layer, and

finally classification of this feature vector. A graphical representation of this data pipeline is

shown in Figure 2.

199
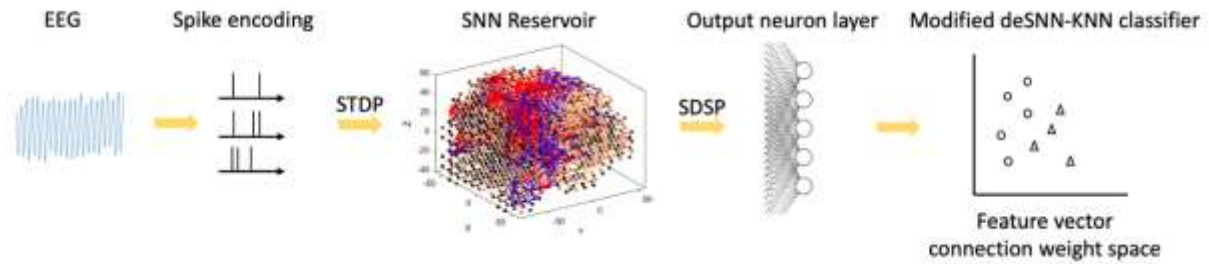
Figure 2. Data pipeline. STDP (spike timing dependent plasticity), SDSP (spike driven

synaptic plasticity), deSNN-KNN (dynamic evolving spiking neural network-k nearest

neighbour algorithm)

Spike Encoding:

SNNs receive reconstructed input signals as binary waveforms known as spike trains. Thus,

the raw EEG data must first be transformed into this format. Step Forward (SF) encoding was

used as a 'signal to spike encoder'. SF is a threshold-based algorithm that works based on

updating cutoff values for excitatory and inhibitory spikes, according to a $base$ value at time

$t = 0$ and a user defined threshold value. If a signal's value is greater than the current

excitatory cutoff ($base + threshold$) then an excitatory spike is encoded, and the excitatory

cutoff value is updated as the new $base$ value. If the signal's value at t is less than the

current inhibitory cutoff value ($base + threshold$) then an inhibitory spike is encoded and

the inhibitory cutoff value is updated as the new base value. In some cases, no spike is

encoded and the base value remains the same[20]. Spike counts for every channel were

extracted and compared between CS and control groups at baseline (A) and during the CS

onset event (B).

NeuCube Reservoir:

A reservoir of connected neurons were initialized in preparation for spike inputs. A SNN

reservoir (SNNr) module is in principle scalable in size, and here it is composed of 1471 LIF

221   neurons representing $1cm^3$ of the brain, located at the same coordinates as those modelled in

222   the Talairach atlas to create a 3D-brain geometry. Defining the spatial location of neurons

223   allows spatial-temporal patterns to be elucidated from spike inputs. Connection weights

224   between reservoir neurons were randomly initialized using the small world connectivity

225   (SWC) approach. The SWC limits connections to only form within a defined radius and the

226   random connections creates a diverse set of dynamical states. Connection weights, also

227   known as 'synaptic weights', modulate any increase or decrease in the membrane potential of

228   the post-synaptic neuron. In other words, it is a measure of the contribution of a pre-synaptic

229   neuron towards the firing of a post-synaptic neuron. Connections also hold an intrinsic value

230   of 'synaptic delay', which is the time delay in firing between pre and post synaptic neurons.

231   Excitatory and inhibitory synapses within the reservoir are probabilistically determined

232   according to the following formula:

233

234 $$P_{i,j} = \begin{cases} C * e^{-(d_{i,j}^{norm}/\lambda)^2} & if \ d_{i,j}^{norm} \leq d_{thresh} \\ 0 & otherwise \end{cases}$$

235

236   Where: $P_{i,j}$ is the probability of establishing a connection between two neurons i and j; C is

237   the maximum connection probability; λ is the small world connection radius; $d_{i,j}^{norm}$ is the

238   normalized distance between two neurons; d_{thresh} is the maximum connection distance

239   between two neurons. In this way, closer neurons have a higher probability of stronger

240   connection weights than neurons further away.

241

242

243

244

245   *SNNr training:*

246   Training the SNNr involved unsupervised learning of spike trains introduced by 'input

247   neurons' at 32 EEG channel locations. These locations were gained from the conversion of

248   10-10 scalp electrode positions into Talairach coordinates. Input neurons feed spike trains of

249   each sample to the SNNr in a temporally synced and spatially distributed manner. Similar to

250   the notion of summation at an axon hillock[21,22], an output spike is produced by a post

251   synaptic neuron when many input spikes from pre synaptic neurons accumulate over a short

252   period of time. As spike trains spread throughout the SNNr, connection weights between

253   reservoir neurons are updated according to a rule called 'Spike Timing Dependent Plasticity'

254   (STDP). The sort of learning mimics cellular processes of long-term potentiation and long-

255   term depression involved in learning and memory[23].

256

257   $$W(s) = \begin{cases} A_+ \, exp[s/t_+] \ for \ s < 0 \\ A_- \, exp[-s/t_+] \ for \ s > 0 \end{cases}$$

258

259   S is the time delay between presynaptic and post-synaptic firing. t_+ is the pre-synaptic time

260   interval. t_+ is the post-synaptic time interval. A_+ is the amplitude of weight increase. A_- is

261   the amplitude of weight decrease.

262   The STDP rule implements a form of logical causality, in which connection weights increase

263   or decrease proportional to the synaptic delay. If a presynaptic neuron fires before a post-

264   synaptic neuron, the connection weight increases between them. Likewise, connection

265   weights decrease if a postsynaptic neuron fires before a presynaptic neuron. The end product

266   is a trained 'SNNr cube' - a neuronal model with connection weights that represent complex

267   and dynamic spatiotemporal brain activity.

268

269

270

271 In our study, the training samples were divided into two groups equally, CS (n=32) and

272 control (n=32). A SNNr cube was trained on all 32 channels of EEG data for each group,

273 giving two distinct SNNr cubes with different connection weights. The connection weights of

274 these cubes were subtracted from each other, producing an SNNr cube specific to
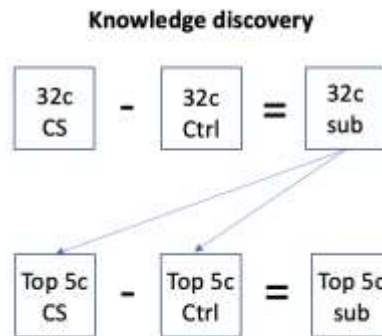
275 cybersickness.

276

277 *Knowledge Discovery:*

278 Subtracted SNNr cubes were made using data 2 seconds in length selected from time

279 segments 30-32s and 90-92s at baseline, and from 1 second before the CS event. Since

280 connections between neurons at SNNr initialization are randomly generated, the same

281 initialized connections were kept constant for subtractions between cybersick and control

282 groups. Underpinning this subtraction, was the hypothesis that there would be different brain

283 information processes and network dynamics in CS versus control subjects. In theory, these

284 differences would not just appear during the manifestation of CS but also during resting-state

285 baseline as a precursor to CS or marker of susceptibility. The reason behind selecting two

286 time points at baseline was to see if these markers might change over time.

287

288 Using the subtracted SNNr cube, clusters of reservoir neurons surrounding each input neuron

289 were grouped by connection weight. Neuron proportion was calculated as the percentage of

290 neurons in the cube belonging to each cluster. Total input cluster interactions were compared

291 to each other in a Feature Interaction Network (FIN) analysis. FIN revealed relative strengths

292 of functionally connected areas of the brain that discriminate between the two classes. The

293 top 5 features (channels) by neuron proportion were chosen as input neurons to train a new

294 SNNr cube, representing only the most informative features that define CS. Data for the

295   control group during VR immersion were selected as the median time of CS induction, which

296   was at the 39 second mark. This process is detailed in Figure 3.

297

298   Figure 3. Finding the top five features to create a new SNNr cube with key CS information; c

299   = EEG channels, CS = cybersickness, Ctrl = Control, sub = subtracted cube

300   *Producing a Feature Vector:*

301   Default NeuCube processing uses one reservoir cube trained on all data samples for

302   classification, with the notion that data of a certain label will have different spike activity and

303   spike propagation than data of another label[24]. This study took a different approach by

304   subtracting individually trained SNNr cubes, to produce synaptic connection weights within

305   the reservoir that form a neural map specific to CS. This map is a template through which

306   new data samples are parsed to obtain a feature vector, which is the synaptic connection

307   weights between input + reservoir neurons, and output neurons. A dynamic evolving SNN

308   algorithm (deSNN) was used to learn the association between class labels and the training

309   samples in a supervised manner. deSNN [15] has the advantage over other SNN classification

310   models in that it is computationally inexpensive and boosts the importance of the order in

311   which input spikes arrives, along with considering all other incoming spikes. Thus, it is

312   suitable for on-line learning and early prediction of temporal events. In this algorithm, a new

313   output neuron (O) for each training sample was created. These output neurons connect to

314   every input and reservoir neuron (N). The connections have initial weights that are set

315   according to the Rank-Order learning rule (RO).

316

$$w_{init}(N_n, O_m) = mod^{order(N_n, O_m)}$$

318

319 The RO learning rule boosts the importance of the first incoming spikes on neuronal

320 synapses. The advantage of RO is fast, one-pass learning and asynchronous data entry of

321 synaptic inputs. The value of the *mod* parameter for part 1 of this study was set to a default of

322 0.9. The O- N connection weights between the SNNr and the output deSNN neurons are then

323 further dynamically tuned by the following spikes via spike driven synaptic plasticity (SDSP)

324 – a modified version of STDP. Due to a bi-stability drift in the SDSP rule, once a weight

325 reaches the defined high value (resulting in LTP) or low value (resulting in LTD), it is fixed

326 for the rest of the training phase. The rate at which a weight reaches LTD or LTP depends on

327 the values of the set *drift* parameter.

328

329 $$w_{final}(N_n, O_m) = \begin{aligned} w_{init}(N_n, O_m) + drift_{up} * n_{spikes} \\ - drift_{down} * n_{spikes} \end{aligned}$$

330

331 $drift_{up}$ is the value increase in synaptic weight after pre-synaptic firing. $drift_{down}$ is the

332 value decrease in synaptic weight with no pre-synaptic firing. $drift_{up}$ is set to 0.08 and

333 $drift_{down}$ is set to 0.08 for part 1 of the study. SDSP works similar to STDP except that the

334 post-synaptic membrane potential is assumed to always reach above threshold when the pre-

335 synaptic neuron fires, leading to an increase in connection weight of the synapse between two

336 neurons. At the same time, if no firing occurs from the pre-synaptic neuron, the connection

337 weight of the synapse is decreased.

338   Altogether, the deSNN algorithm provided brain-inspired feature vectors for every sample,

339   consisting of both input-output neuron connections, and reservoir-output neuron connections

340   that can be classified.

341

342   The following connection strategies between the SNNr neurons and the deSNN classifier

343   neurons were explored in this paper while searching for an optimal model:

344   -   SNNr cube trained on all data of 32 input neurons; 1471 SNNr neurons connected to

345   each output neuron in the evolved deSNN classifier;

346   -   SNNr cube trained on all data of 32 input neurons; only the 32 input neurons are

347   connected to the output neurons;

348   -   SNNr cube trained on 5 channel data; 1471 SNNr neurons connected to each output

349   neuron in the evolved deSNN classifier

350   -   SNNr cube trained on all data using all combinations of 5 top input neurons (e.g. top

351   channels); only the 5 input neurons are connected to each output neuron;

352

353   *ECG*

354   The following heart rate variability parameters were computed: PNS, SNS, SI, SDNN,

355   RMSSD. The selected time segments were 2 minutes, 30s and 10s in length. Only RMSSD

356   was analysed for the 10s time segments, due to the statistical unreliability of the other

357   parameters for this length of data. RMSSD is considered a reliable indicator for

358   parasympathetic cardiac activity robust to the signal noise of respiration. Meanwhile, SI is an

359   index for sympathetic activity Both parasympathetic and sympathetic activity contribute to

360   SDNN. PNS and SNS are validated indicators of parasympathetic and sympathetic

361   activity[25,14].

362

363   *Classification*

364   Three different algorithms were used to classify the feature vectors, with leave-one-out cross

365   validation (LOOCV):

366

367   *Modified KNN:*

368   A distance-based algorithm between data points. The study employed a modified version of

369   KNN, in which the following parameters were optimized using an exhaustive grid search:

370   1)   k is for all neighbours or restricted by class label;

371   2)   Using Manhattan distance or Euclidean distance;

372   3)   Distance initially weighted uniformly or by signal-to-noise ratio (SNR) that identifies

373   the importance of the features (see the wwkNN method [37]);

374   4)   Neighbours weighted during voting –

375   a.   Uniform (equally)

376   b.   By the inverse of their distance

377   c.   By the function: $\frac{\max distance - (neighbour - minimum\ distance)}{\max distance}$

378   5)   Feature weights weighted during voting –

379   a.   Uniform for each feature

380   b.   SNR for each feature

381

382   *Linear Discriminant Analysis (LDA):*

383   An algorithm that finds linear combinations of features that separate classes along a

384   hyperplane. Least squares solution was used with optimized shrinkage.

385

386   *Light Gradient Boosting Machine (LightGBM)*:

387   LightGBM is a gradient boosting framework that uses tree-based learning algorithms.

388   Optimized for number of trees, learning rate, boosting type (gradient boosting decision tree,

389   GBDT), gradient-based one-side sampling (goss), dropouts meet multiple additive regression

390   trees (dart)).

391

392   This study approached data fusion by combining feature vectors representing synaptic

393   connection weights with the output layer of NeuCube and HRV variables that yielded the

394   best accuracies. These include the best combination of parasympathetic or sympathetic

395   features which would be added on to the final feature vector.

396

397   Part 2 of the study used high capacity computing provided by New Zealand eScience

398   Infrastrucutre (NeSI) to extend the previous analysis using the modified KNN algorithm. The

399   goal was to find the best time segment for prediction out of the 2 minute EEG resting-state

400   baseline, partitioned into varying data lengths (2s, 5s, 10s). The analysis similarly scans

401   through all types of model training, and feature vector type in terms of connections to the

402   output neurons as in Part 1. The difference is that *mod* and *drift* parameters for SDSP were

403   optimized for classification of the best time segment for prediction and also for detection to

404   see if this would improve accuracy. Additionally, the value of $drift_{up}$ was set to always be

405   more than $drift_{down}$, which implements stronger I-O connection increases compared to

406   decreases. This type of SDSP also maintains stronger I-O connections for input neurons that

407   fire more compared to those that fire less, thereby boosting their importance further. Varying

408   data lengths serve to explore whether capturing more EEG data improves prediction

409   accuracy, whereas optimizing for SDSP improves the transformation of the EEG data into the

410   feature vector for classification.

411

412   **Results**

413   **Part 1**

414   *MSSQ-short and SSQ Scores*

415   MSSQ-short scores did not differ significantly (P>0.05) between CS and Control groups

416   (Figure 4). SSQ scores differed significantly between CS and control (P>0.0001) (Figure 5).

417   CS groups had significantly higher SSQ scores than controls, showing that MSSQ-short

418   percentile scores were not a good indicator of sickness in VR usage.
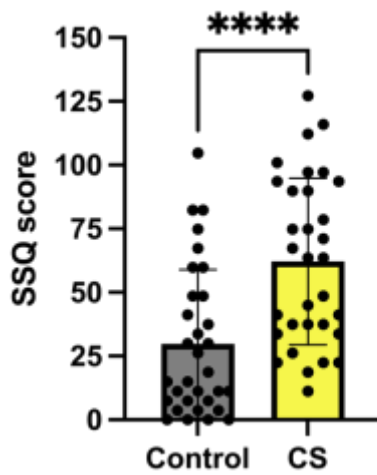
419
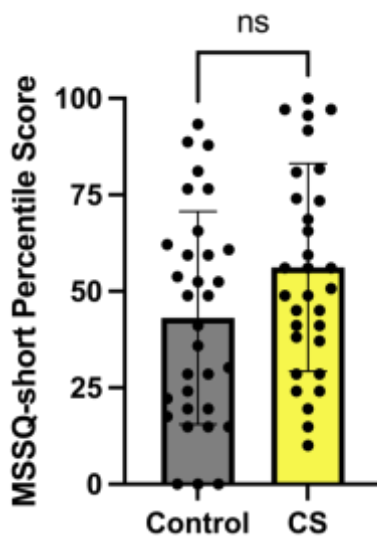
420
421
422   **Figure 4**. MSSQ-short scores P>0.05. Error bars show ± SEM.
423
424

425
426
427   **Figure 5**. SSQ scores, **** = p>0.0001. Error bars show ± SEM.
428

429   *EEG*

430   Functional connectivity analysis at resting baseline EEG (30-32s) shows that CS prone

431   individuals have more concentrated negative connections in the Cz area, interspersed with

432   surrounding positive connections (Figures 6a and 6b), when compared to controls. Feature

433   interaction analysis (FIN) revealed that Cz is likely a hub for brain activity processing in this

434   time segment, either collecting or sending out this information to all the other key channels

435   located in the left and interhemispheric frontal and bilateral parietal areas (Figure 6c and 6d).

436   The top 5 features according to neuron proportion were P4, Fz, Cz, PO3 and F3, with Cz

437   being the highest (Figure 7). A second time segment further on in the baseline (90-92s) was

438   analysed, which showed that other important features (T8, CP6, Fz, FC5, T7) can appear at

439   different time segments (Figure 8 and Figure 9). During the CS event, the high functional

440   connectivity seen at baseline in CZ changes to interspersed positive and negative

441   connections. Meanwhile there is a shift towards O2 positive connection dominance. FIN

442   analysis (Figure 10) showed that both O2 followed by Cz are most likely hubs for

443   cybersickness processing, where both have the highest neuron proportion (Figure 11). The

444   top 5 features according to neuron proportion were FC6, FP2, FP1, Cz and O2. These results

445   indicate that important areas identified in the baseline that are also found during the

446   manifestation of cybersickness could be important biomarkers of susceptibility to
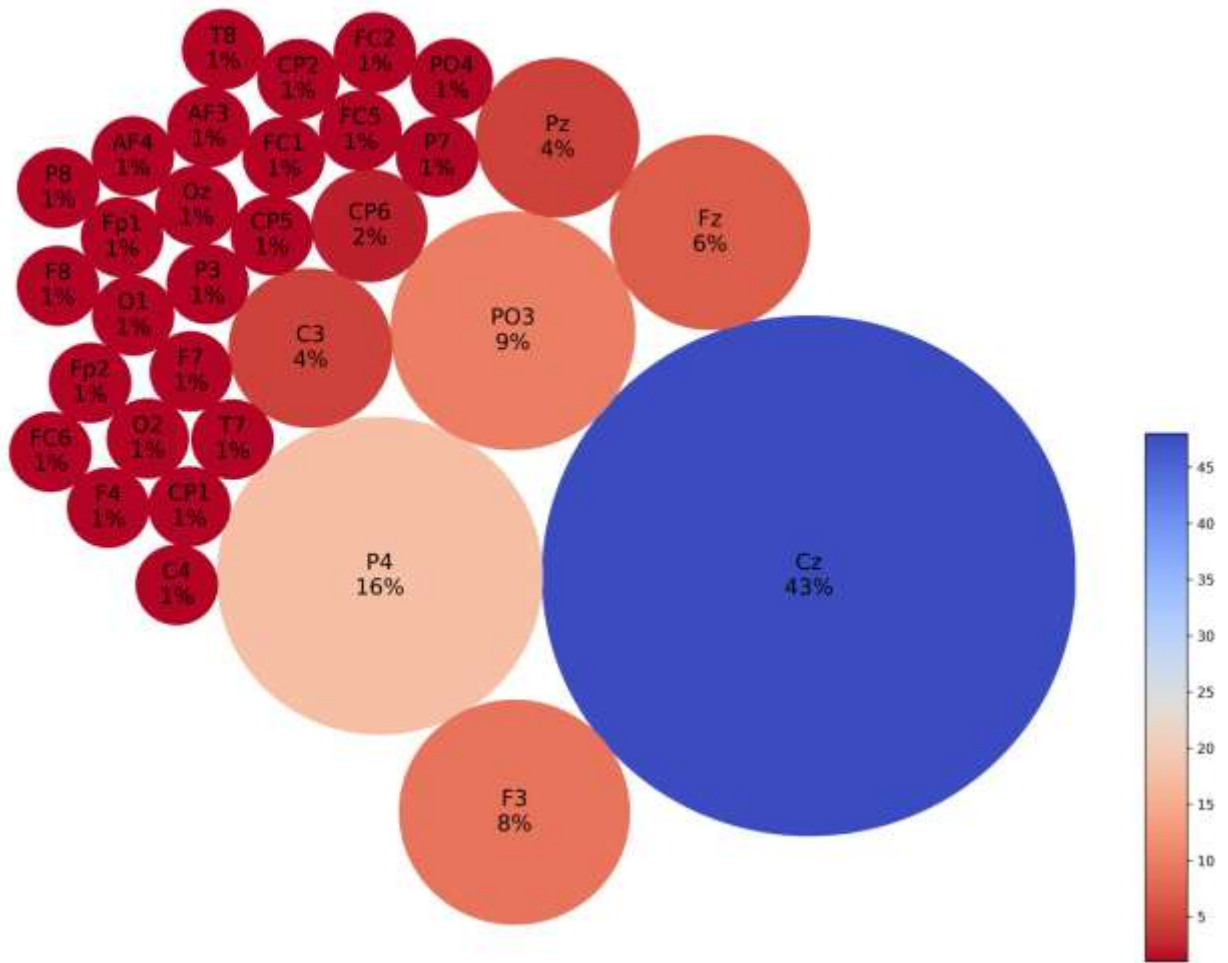
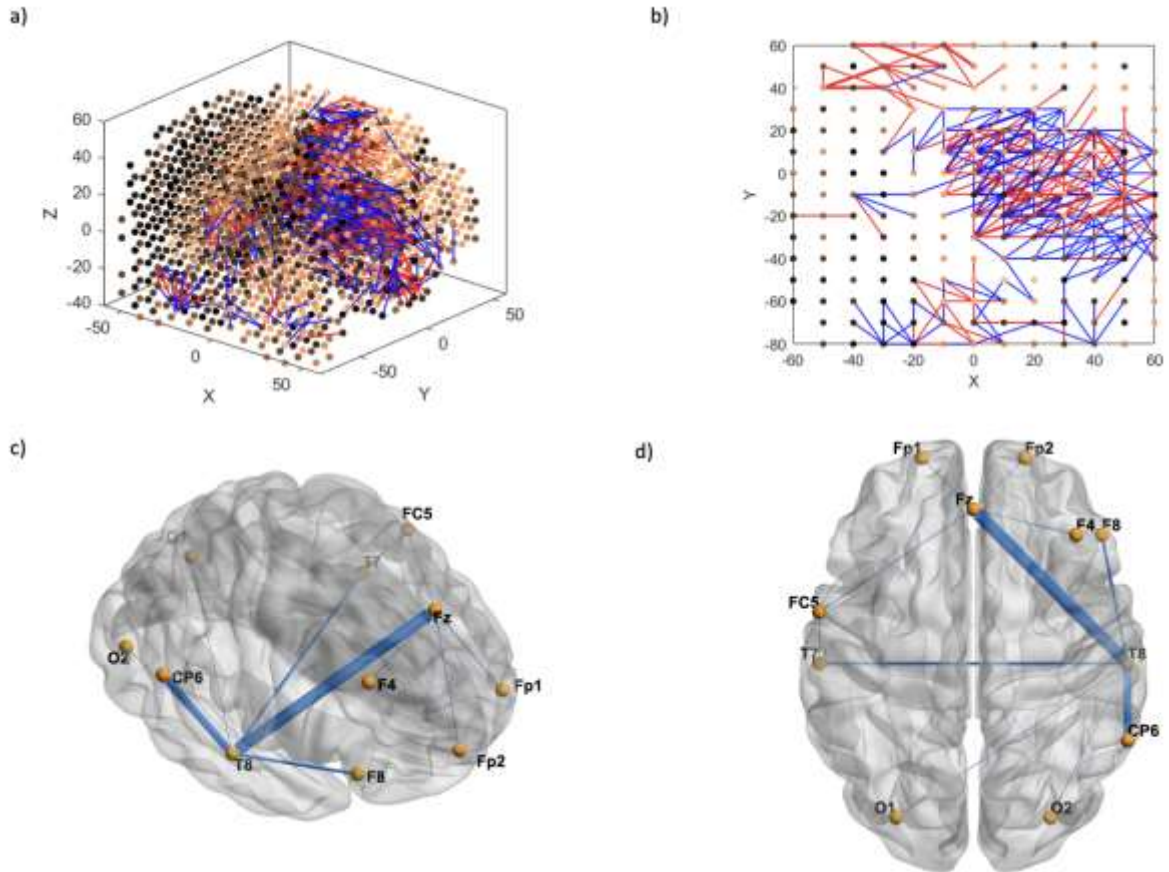447   cybersickness.

448

449

450

451
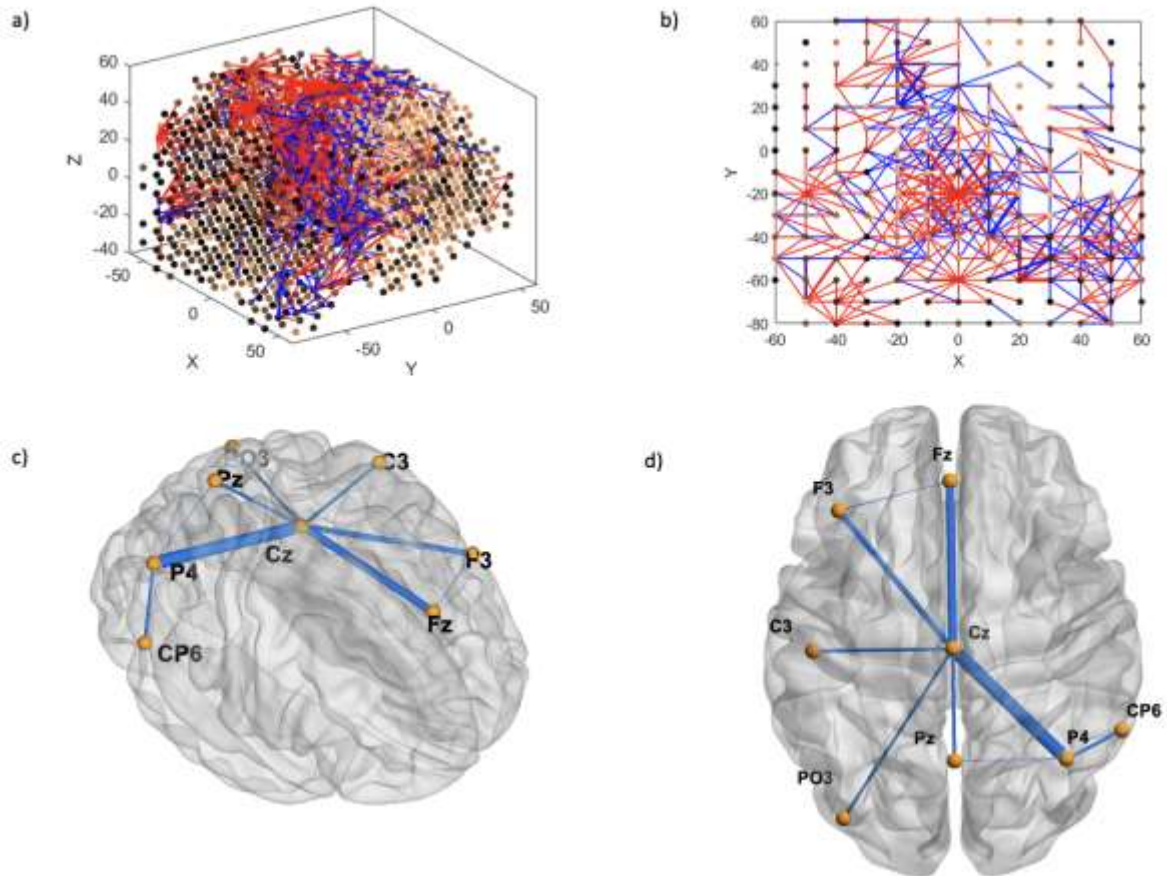
Figure 6. Resting-state baseline 30-32s subtracted network dynamics. Functional connectivity of neurons in the SNNr is represented by **a)** right hemisphere medial view of the SNNr and **b)** axial view. Blue lines are positive connections, red lines are negative connections. Brighter neurons have stronger connections. Feature interaction networks between channels are represented by **c)** right hemisphere medial view and **d) axial view.** Thicker lines indicate stronger interaction whether they be positive or negative. *These interactions confirm our hypothesis that even at baseline of 30-32s, there is a significant difference between the brain information processes of CS versus control subjects.*

Figure 7. Neuron proportion clustered by connection weights in the subtracted SNNr = SNNr/control – SNNr/cs at resting-state baseline 30-32s. Blue indicates higher proportion, red indicates less neuron proportion. It shows a larger difference between the CS and control subjects in the brain areas Cz, F3, P4, PO3, Fz, Pz and C3, with a dominant factor of Cz.

Figure 8. Resting-state baseline 90-92s subtracted network dynamics. Functional connectivity of neurons is represented by **a)** right hemisphere medial view and **b)** axial view. Blue lines are positive connections, red lines are negative connections. Brighter neurons have stronger connections. Feature interaction networks between channels are represented by **c)** right hemisphere medial view and **d) axial view.** Thicker lines indicate a stronger interaction whether they be positive or negative. *These interactions confirm our hypothesis that even at the 90-92 baseline, there is a significant difference between the brain information processes of CS versus control subjects.*

489
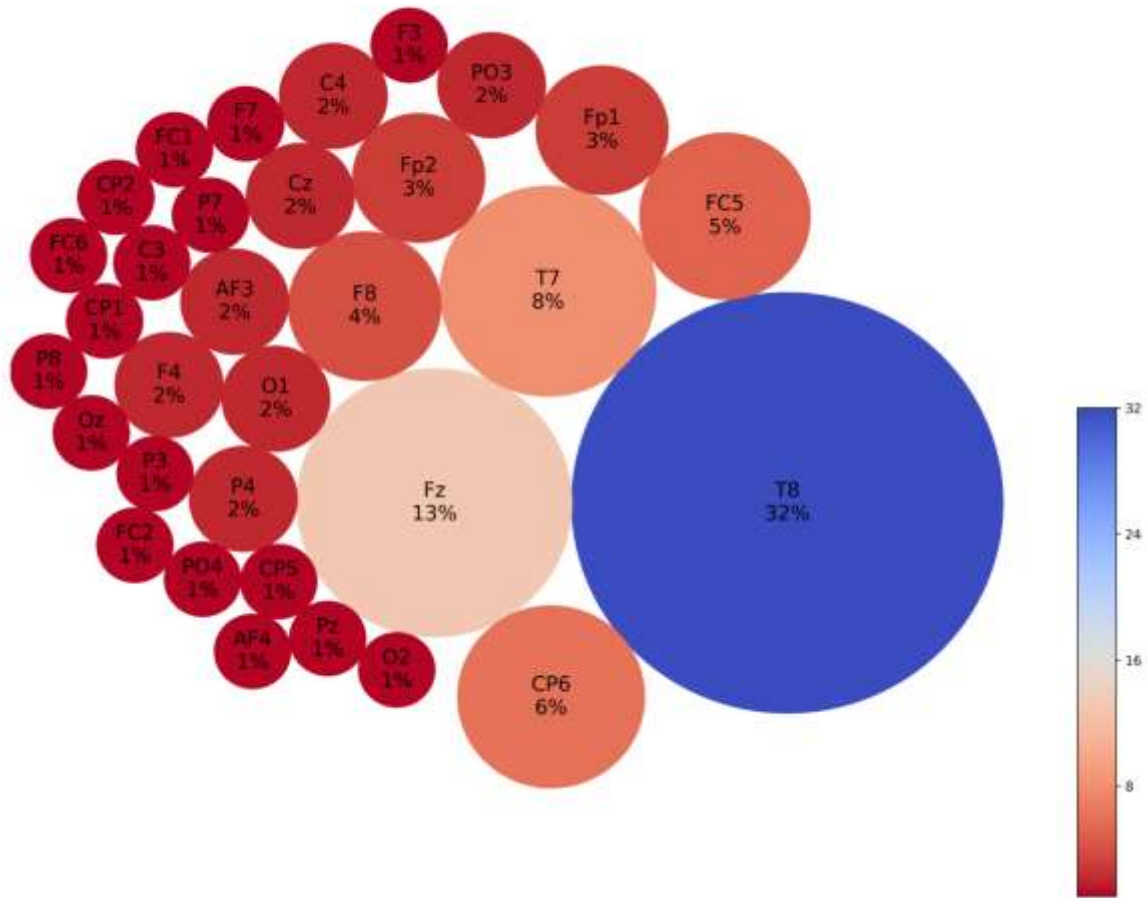
Figure 9. Neuron proportion clustered by connection weight at 90-92s resting-state baseline. Blue indicates higher proportion, red indicates less neuron proportion. It shows a larger difference between the CS and control subjects in the brain areas T8, CP6, Fz, T7, FC5 with a dominant factor of T8.

490
491
492
493
494
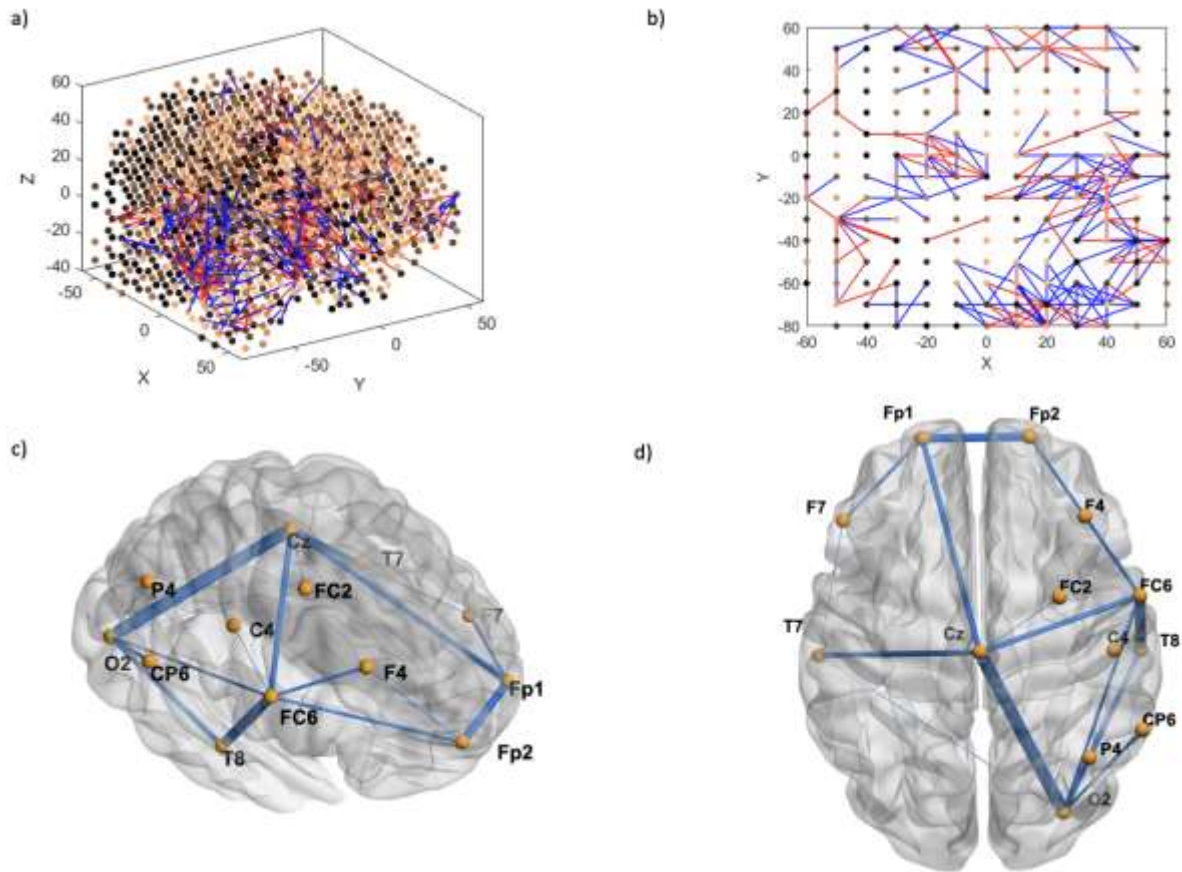
Figure 10. Cybersickness network dynamics of the SNNr=SNNr/control – SNNr/cs, in VR. Functional connectivity of neurons is represented by **a)** medial view) and **b)** (axial view). Blue lines are positive connections, red lines are negative connections in **a) and b)**. Brighter neurons have stronger connections. Feature interaction networks between channels are represented by **c)** and **d).** Thicker lines indicate stronger interaction whether they be positive or negative. *These interactions confirm our hypothesis that there is a significant difference between the brain information processes of CS versus control subjects during the CS manifestation when subjects are exposed to VR. Some of these interactions have been captured already at baseline (see Fig.6 and Fig.8).*

Figure 11. Neuron proportion in SNNr = SNNr/control – SNNr/cs, clustered by connection weights during a VR experiment. Blue indicates a higher proportion, and red indicates a lower proportion of neurons. *The difference in the connectivity confirms our hypothesis that there is a significant difference between the brain information processes of CS versus control subjects during the CS manifestation, 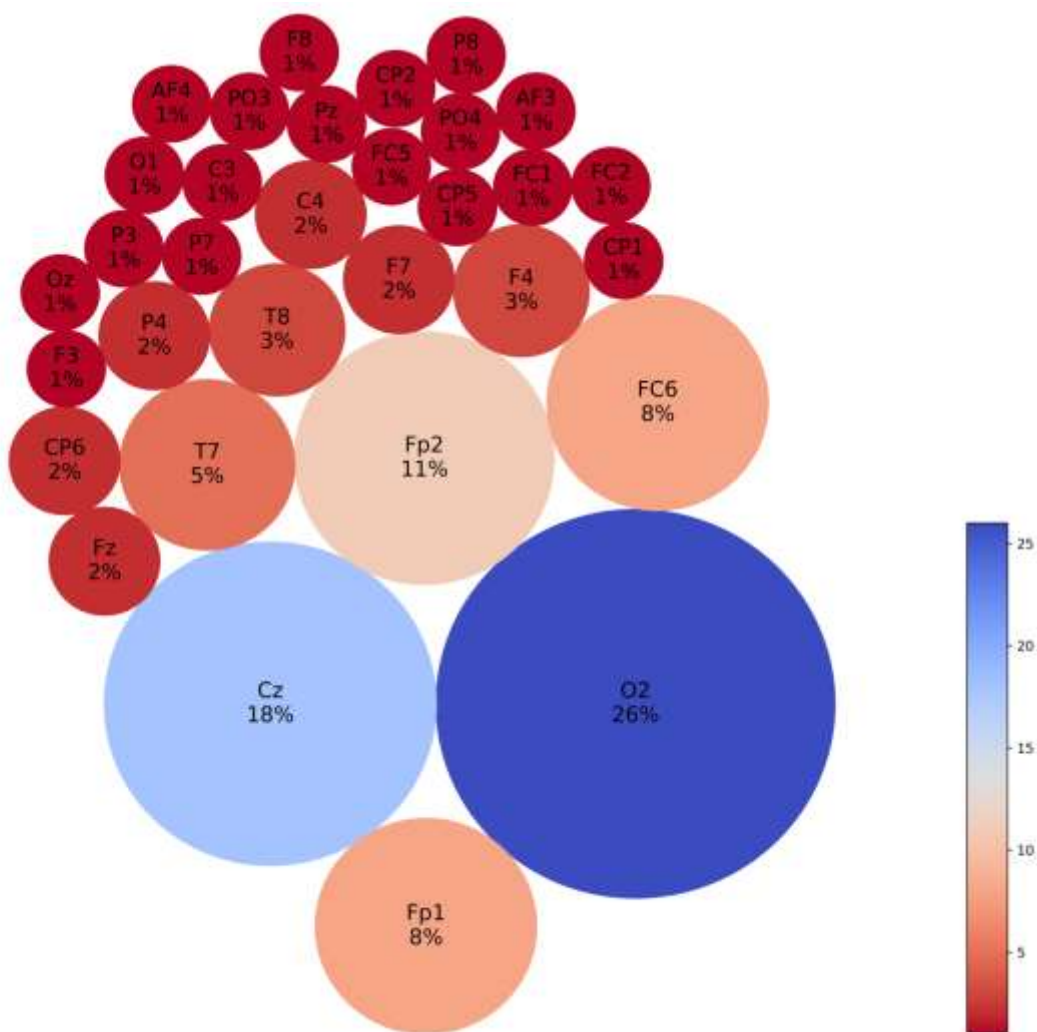when subjects are exposed to VR, with dominating brain areas being O2, Cz, Fp2, Fp1 and Fc6. Some of these areas have been captured already at baseline (see Fig.7).*

Classification results

Overall, our modified KNN algorithm was the best for both prediction (EEG 76.6%, ECG 74.2%) and detection (EEG 75%, ECG 72.6%) of CS (Tables 1-5 and Figure 12). Both EEG and ECG had similar classification accuracies, although EEG alone was slightly better. Although data fusion of both EEG and ECG could increase accuracy to 77.4% for prediction, it reduced the accuracy for detection to 70.9% (Figure 12).

	Prediction 30-32s					
I-O connection	32 Channel Trained			5 Channel Trained		
	LDA	KNN	LGBM	LDA	KNN	LGBM
1471 Reservoir + I-O	59.4%	65.60%	68.8%	53.1%	67.20%	53.1%
32	62.5%	67.20%	62.5%	N/A	N/A	N/A
5	54.7%	60.90%	54.7%	59.4%	73.40%	59.4%
P4	48.4%	65.60%	57.8%	46.9%	51.60%	51.6%
Fz	50.0%	59.40%	46.9%	57.8%	70.30%	70.3%
Cz	43.8%	60.90%	57.8%	39.1%	60.90%	54.7%
PO3	0.00%	57.80%	48.4%	0.00%	57.80%	54.7%
F3	53.1%	62.50%	62.5%	53.1%	64.10%	64.1%
Best combo out of 5	Cz+F3 56.3%	P4, Fz, Cz 75.00%	P4, PO3 64%	Cz+F3 62.5%	Fz, Cz **76.6%**	Cz 70.3%

Table 1. Prediction accuracies of LDA, modified KNN and LGBM classification algorithms at baseline 30-32s for all subtracted SNNr Cubes.

	Prediction 90-92s					
I-O connection	32 Channel Trained			5 Channel Trained		
	LDA	KNN	LGBM	LDA	KNN	LGBM

	32 Channel			5 Channel		
	LDA	KNN	LGBM	LDA	KNN	LGBM
1471 Reservoir + I-O	53.1%	67.20%	60.9%	50.0%	65.60%	73.4%
32	57.8%	70.30%	64.1%	N/A	N/A	N/A
5	51.6%	68.80%	70.3%	54.7%	64.10%	68.8%
T8	48.4%	71.90%	60.9%	50.0%	62.50%	56.3%
CP6	59.4%	54.70%	56.3%	56.3%	64.10%	67.2%
Fz	50.0%	60.90%	59.4%	0.00%	64.10%	54.7%
FC5	18.8%	60.90%	56.3%	42.2%	60.90%	54.7%
T7	23.4%	65.60%	53.1%	42.2%	57.80%	54.7%
Best combo out of 5	T8+CP6+Fz 59.4%	T8 73.40%	T8 61.3%	T8,CP6,Fz, FC5 57.8%	T8, CP6 **75%**	T8,CP6 66.1%

Table 2. Prediction accuracies of LDA, modified KNN and LGBM classification algorithms at baseline 90-92s for all subtracted SNNr Cubes.

Detection CS onset						
I-O connection	32 Channel Trained			5 Channel Trained		
	LDA	KNN	LGBM	LDA	KNN	LGBM
1471 Reservoir + I-O	57.8%	70.30%	75.0%	56.3%	57.80%	65.6%
32	65.6%	**75.00%**	70.3%	N/A	N/A	N/A
5	50.0%	62.50%	67.2%	53.1%	62.50%	60.1%
FC6	59.4%	65.60%	62.5%	53.1%	67.20%	65.6%
Fp2	42.2%	56.30%	59.4%	43.8%	59.40%	59.4%
Fp1	46.9%	60.90%	57.8%	0.00%	64.10%	59.4%
Cz	25.0%	56.30%	54.7%	53.1%	56.0%	64.1%
O2	51.6%	53.10%	45.3%	0.00%	50.0%	59.4%
Best combo out of 5	FC6 59.4%	Fp2, Cz 68.80%	Fp1,Cz 68.8%	FC6+Fp2+Cz 57.8%	Fp2, Cz 68.80%	FC6,Fp1,Cz 68.8%

Table 3. Detection accuracies of LDA, modified KNN and LGBM classification algorithms at the time of the CS event for all subtracted SNNr Cubes.

540

541

ECG Prediction			
Time Segment	ML Algorithm		
	LDA	KNN	LGBM
2 Min Baseline	56.5% SI+SDNN	**74.2%** PNS+SNS	69.4% SNS
15-45s	61.3% PNS + SNS +SDNN + RMSSD	67.7% SI	67.7% SNS + SI + RMSSD
75-105s	62.9% PNS + SNS	**74.2%** SNS	71.0% SNS +SDNN
25-35s	6.5% RMSSD	67.7% RMSSD	61.3% RMSSD
85-95s	16.1% RMSSD	59.7% RMSSD	51.6% RMSSD

542

Table 4. Prediction accuracies of LDA, modified KNN and LGBM classification algorithms

at different time segments for the best combination of HRV parameters.

545

ECG Detection			
Time Segment	ML Algorithm		
	LDA	KNN	LGBM
2 Min VR	61.3% (PNS or SDNN) + SNS + Mean HR	**72.6%** SNS+SI	69.4% SI + SDNN
30s VR	66.1% PNS + SNS +SI	69.4% PNS + SNS + SI/ PNS + SI + RMSSD	67.7% SI + SDNN + Mean HR
VR 10s	56.5% RMSSD	58.1% RMSSD	54.8% RMSSD

546

Table 5. Detection accuracies of LDA, modified KNN and LGBM classification algorithms

at different time segments for the best combination of HRV parameters.

549

550

551 **Figure 12**. Best KNN classification accuracies for EEG and ECG (HRV) in multiple time

552 segment analyses.

553

554 *EEG considerations*

555 Some participants were predicted at 30-32s (samples 3, 4, 18, 24, 27) but not at 90-92s and

556 vice versa (samples 9, 22 and 23). A hypothesis was that spike count, MSSQ-short percentile

557 scores, SSQ total scores, or CS onset times could explain why some participants were

558 predicted in one baseline segment but not the other. This was not the case, as none of the

559 above showed any deviation from the norm when graphed (appendix 1-6).
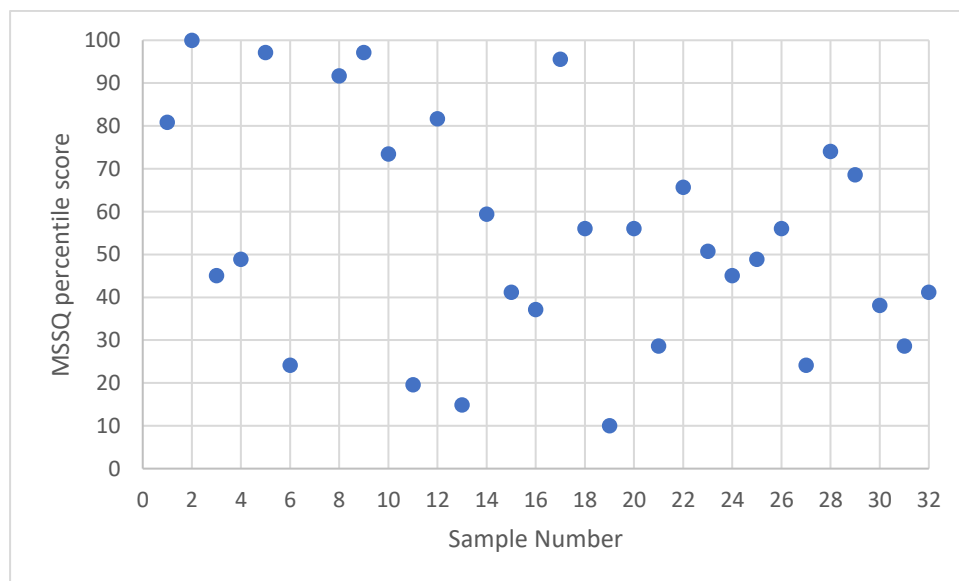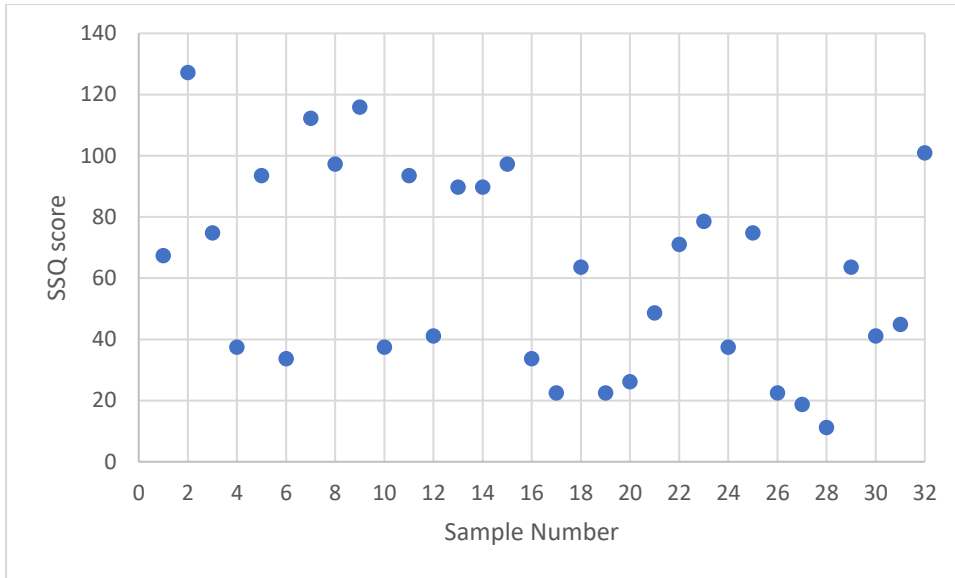

560
561
562 Appendix 1. MSSQ percentile score breakdown for the CS group.
563

564
565
566   Appendix 2. SSQ score breakdown for the CS group
567
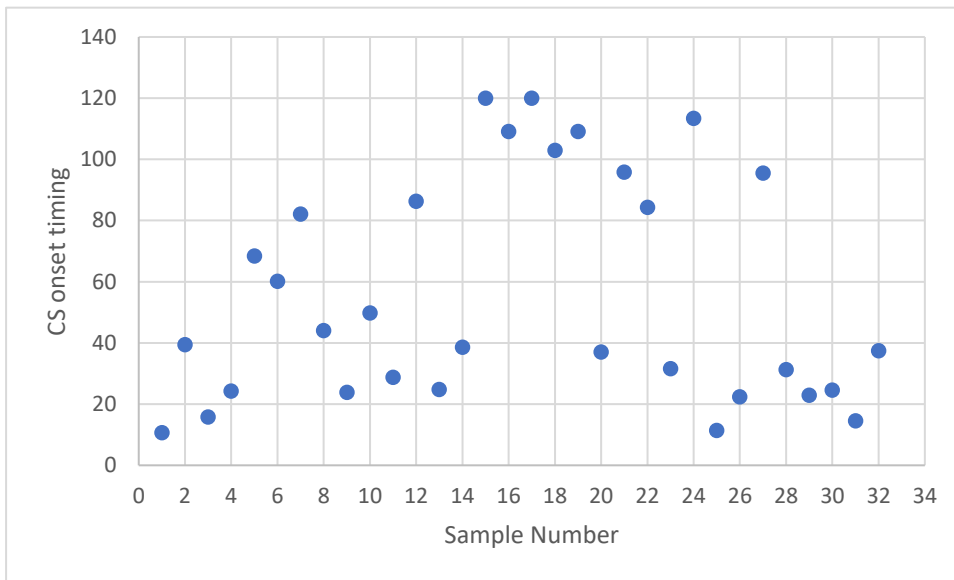
568
569
570
571
572
573
574
575
576
577
578
579
580
581
582
583
584

585
586   Appendix 3. CS onset timings
587
588

589
590
591
592
593
594
595
596
597
598
599
600
601
602
603
604
605

606 Appendix 4. Spike count of 30-32s time segment for all CS participants. Sample number 3, 4,
607 18, 24 and 27 were predicted at 30-32s but not at 90-92s.

608
609
610
611
612
613
614
615
616
617
618
619
620
621
622
623
624
625
626
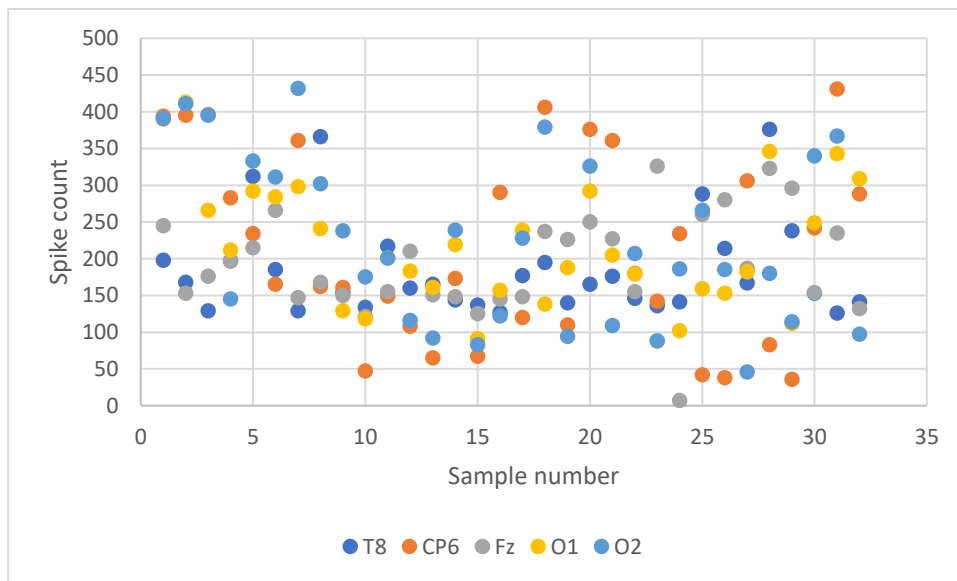
627 Appendix 5. Spike count of 90-92s time segment for all CS participants. Sample number 9,
628 22, 23 were predicted at 90-92s but not at 30-32s.

629
630

Appendix 6. Spike count for all CS participants during the CS onset.

It was hypothesized that the spike count at each channel would be different in the CS groups

compared to controls at all time segments. We found that the spike count was significantly

lower in the CS group than in the controls at the 30-32s baseline segment (for P4, Fz, Cz

PO3, F3) and during VR immersion (O2) ($P<0.0001$), but not at 90-92s. Sample 7 in 30-32s

has a high spike count compared to others, as does sample 10 during VR immersion, but
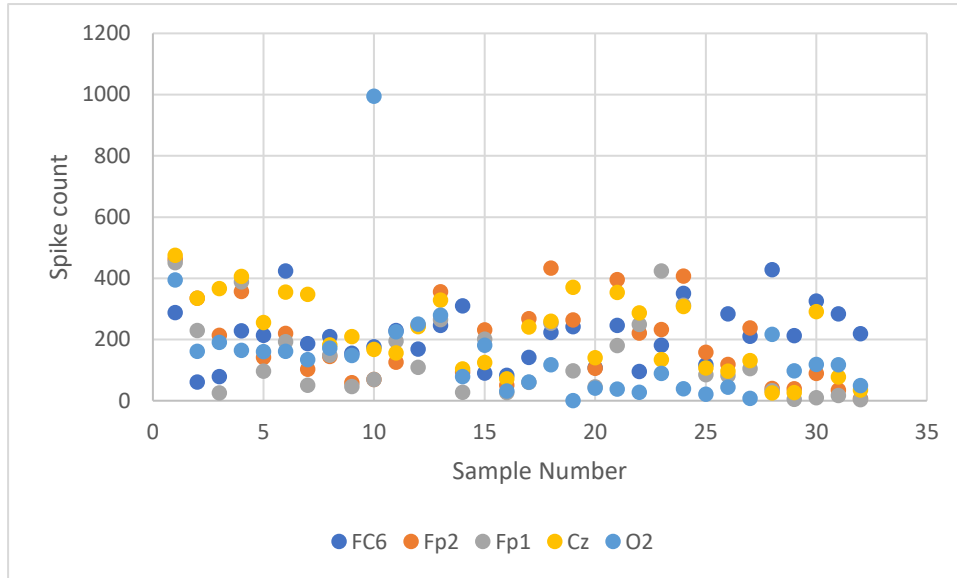
removal of these samples does not change the statistical differences (30-32s $P<0.0001$, VR

immersion $P<0.001$) between CS and controls spike count. Classification accuracy, however,

remains similar for 30-32s and 90-92s analysis (76.6% and 75.0%, respectively).

ECG and HRV considerations

Sympathetic indexes (SNS + SI) outclassed other HRV parameters in terms of classification

accuracy. A normal control baseline may be easy to predict or detect, but small changes in

these HRV values may not always equate to cybersickness. The differences between CS and

Ctrl groups must be more complicated than just their means, medians and distributions,

because as a whole, there are no significant differences ($p>0.05$) between any of the HRV

665 parameters used here according to a Mann Whitney u rank test. Furthermore, both of the

666 KNN algorithms employed here employ a min/max voting type on the importance of K-

667 neighbours, which takes into account a weighted Euclidian distance via signal to noise ratio

668 (SNR) between sample data points. These weightings between all data points and between K-

669 neighbours are still influenced by the sample sizes and distribution of the data. Therefore, it

670 may also be possible that a larger sample size is needed to more accurately represent

671 cybersickness.

672

673 **Part 2**

674 After extensive analysis of different time segments and data lengths, the 2 second time

675 segment relating to 110 - 112 seconds, with only one of I-O connection (F7 channel), yielded

676 the best results of 85.9% accuracy. Overlapping time segments for data lengths 5s and 10s

677 did not reach the same performance, achieving a max 75-76% using the best combination of

678 I-O connections. In addition, detection performance was boosted to 76.6% after SDSP

679 optimization.

680

	EEG	EEG + ECG Fusion
Prediction	85.9% (F7)	74.2% (75-105s, SNS)
Detection	76.6% (FP1, Cz)	72.6% (2 mins, SNS + SI)

681

682 Table 6. Improved accuracies for CS prediction and detection using EEG. Analysis included

683 time segment and data length optimization (prediction only), and SDSP optimization of the

684 *mod*, *driftup* and *driftdown* parameter. Fusion accuracies increased for detection but not for

685 prediction.

686

687

Discussion

Classification

This paper presents a proof of concept for on-the-spot prediction of cybersickness at resting state baseline and near-instant detection of cybersickness during its onset. The algorithms are based on brain inspired SNN architectures and HRV classification. Another study has also demonstrated the predictive capacity of their algorithm for CS at resting baseline with a smaller sample size of n=19[26]. Near-instant detection was demonstrated by Nam et al. [27] but required PCA preprocessing, power spectral analysis for EEG and 7 other biosignals. The present study shows that only 2 seconds of EEG data and 30 seconds of ECG data are required, and both biosignals can be used individually or together to predict and detect CS. The modified deSNN-KNN classification algorithm produced the best results in terms of accuracy, over LDA and light-GBM. It was found that similar classification accuracies can be obtained by using either earlier (30-32s, 76.6%) or later time segments (90-92s, 75%) at baseline. Upon further investigation, the study found that time segment optimization was still important (85.9%). Simplifying feature vectors by removing reservoir – output neuron connections, and leaving the direct connections of input neurons to output neurons increases accuracies (Table 1-3). In addition, reducing redundancy in training data by focusing on key cybersickness relevant areas also has the same positive effect on accuracy. However, in the case where a model is trained on all 32 features, but only the top 5 features are considered, a reduction leads to a decrease in accuracy (75.00% to 68.80%) (Table 3). This highlights that in idealistic scenarios, not just a few but all features a model is trained on should be considered when eliminating redundancy. However, it is important to note that there is a trade-off in considering all features, as computational cost increases when conducting exhaustive searches.

712

713 Our analysis did not reveal why some participants were predicted in one baseline segment but

714 not the other. An explanation is that this could be due to differences in the temporal

715 characteristics of the spiking activity of neurons captured by the connection weights between

716 input clusters and between individual reservoir neurons. Another explanation could be due to

717 the nature of clinical studies, where there is interindividual variation between participants.

718

719 Fusion of EEG and ECG did not yield much improvement in accuracy, and in the case of

720 detection it worsened accuracies in part 1. Multi-modal data fusion was investigated to

721 explore if information from two organs would lead to increased accuracy, especially because

722 they are biologically linked through the nervous system both in anatomy and also in

723 association to nausea[28]. Because of the disparity in classification performances between

724 EEG and ECG, it is likely that the classification algorithm's ability to differentiate strongly

725 between labels is 'drowned' out by the ECG HRV features, which is why the EEG now adds

726 no useful information for classification beyond what is already there. It is also possible that

727 KNN being a distance based algorithm, gets worse with higher dimensional feature vectors, a

728 trend shown as well in the improved classification performances the less features there are in

729 the feature vector.

730

731 *MSSQ and SSQ scores*

732 In our experiment, the MSSQ-short was not a good predictor of cybersickness induction or

733 sickness ratings. This points towards the need for questionnaires more targeted at visually

734 induced motion sickness[29] to assess susceptibility. SSQ scores were a good adjunct to the

735 subjective cybersickness reports in the separation of cybersick and control groups.

736

737   *Related spatiotemporal brain dynamics were discovered in the following* areas:

738   Fz Brodmann 8 visual attention and eye movements

739   T8, T7: Auditory processing

740   CP6: Auditory processing, speech comprehension

741   O1, O2: Retinotopic mapping of visual scene, edge detection

742   P4: Angular gyrus attention, memory retrieval, language number processing, spatial

743   cognition

744   PO3: Associative visual cortex (V3, V4, V5).

745   F3: Frontal eye fields, visual attention and eye movements.

746   FC5, FC6: Brocas speech production and articulation (primarily left hemisphere),

747   language processing.

748   FP1, FP2: Executive function, decision making

749   F7, F8: Active maintenance of stimulus information, interoceptive, limbic emotion-

750   motivational, and sensory input integration

751   CS is a complex condition with many brain areas involved[30,31]. Presented in this study is

752   functional connectivity of the brain that predicts future CS, meaning that an individual with

753   similar neural maps may be susceptible to cybersickness, and connectivity that marks the CS

754   event. In the present study, a high neuron proportion grouped by connection weight of frontal

755   (FC6, FP1, FP2) regions during the CS event, and temporal regions (T8) during resting

756   baseline are consistent with another study showing changes in these areas well into the CS

757   event. In addition, areas involved in CS include those for visual + attention processing and

758   executive function (CP6, O2, PO3, F3, F4, FP1, FP2). Liu et al. [30] found reduced

759   gravitational frequency means (transition of EEG power spectral density, temporal changes

760   within a frequency band), and gravitational frequency standard deviation (dispersion of brain

761 signal) at FP1, FP2, TP9 and TP1. Power spectral entropy (disorder of time sequence signals

762 and irregularity of multi-frequency component signals) and Kolmogorov complexity (time

763 domain complexity) were all reduced at FP1 and FP2 during VIMS[30]. However, it was

764 noted that these changes may be related to other factors, such as alertness level or various

765 mental conditions, and not limited or specific to VIMS. Our finding of an increase in O2's

766 interaction with other areas during cybersickness highlights that visual processing is altered

767 beyond just the demands of normal visual processing in VR. O2 has been selected as an

768 important feature in other machine learning studies as well [27,32,33], but the possible

769 differences in results compared to the discussed brain analysis and imaging studies may be in

770 the temporal specificity (2 seconds long) of our analysis compared to longer data lengths

771 analysed.

772

773 Of interest is the brain activity hub found at Cz, which had altered connectivity at resting-

774 state baseline as well as during the onset of cybersickness when compared with controls.

775 Reduced spike count at Cz before VR immersion may indicate that there is less frequency of

776 communication from this area to other connected areas. Cz interacts with three cortices

777 simultaneously, the somatosensory, motor and also is positioned over the mid cingulate,

778 which has increased functional connectivity with the left V5/MT during cybersickness[34].

779 Krokos, Varshney [35] found high activity power in the central regions similar to the location

780 of Cz, of average scalp maps according to independent component analysis. Brodmann area 5

781 corresponds to Cz, which is part of the superior parietal lobule and post central gyrus. It is

782 located immediately posterior to the primary somatosensory cortex. Neuroimaging evidence

783 suggests that this area contributes to movement planning. Furthermore, one study showed a

784 correlation between the activity of area 5 neurons and the starting or final coordinates of limb

785 movement. This suggested that BA5 is involved in processing spatial information for limb

786   movement. Emerging evidence suggests that BA5 is also involved in the inhibition of

787   movement[36]. A transcranial magnetic stimulation study found a causal role for BA5 in the

788   regulation of corticospinal output during preparation that differentiates between whether a

789   movement is withheld or executed[37]. One may think that Cz's role in movement and also

790   as a marker of future cybersickness at resting baseline lends possible credence to the postural

791   instability theory of motion sickness, which postulates that postural instability is both a

792   marker and a predictor of motion sickness, likely extending as well to cybersickness in virtual

793   reality[38]. Our results, however, suggest that although processes related to motor control are

794   altered during the event, we cannot speak for postural instability itself. Furthermore, a recent

795   study shows that postural instability itself is not a good predictor of cybersickness. For purely

796   visually induced motion sickness (VIMS), increases in functional connectivity were also

797   found between the right MT/V5 and anterior insula. Decreased functional connectivity was

798   also found between the left and right V1[34]. The left MT/V5 in particular is an area

799   important for processing of "what" but not "where", in priming for motion direction but not

800   spatial position[39]. Nonetheless, cortical areas that control movement and visual processing

801   are clearly involved in cybersickness.

802   Interestingly, cortical areas for visually induced cybersickness also overlap with areas

803   involved in vestibular processing: Cz and FC6 – premotor and supplementary motor

804   (movement processing, planning and inhibition) and P4 – medial superior temporal (motion

805   detection). In this study, it can be observed that the size of the nodal cluster and strength of

806   connectivity shift to right hemispheric dominance during CS, a preference also observed in

807   vestibular processing. Overall, there appears to be an alteration of activity and connection in

808   areas related to motor control and planning, as well as visual processing. These areas may

809   become targets of intervention for future studies. [40]

810

811   F7 was highlighted as an area of interest after its correlation as an input to produce high

812   accuracies in part 2 of the analysis. F7 relates to Brodmann area 45, the inferior frontal gyrus

813   (IFG) [41]. The IFG and also anterior insular (AI), which also has associations with V5/MT

814   as described above, is part of the ventrolateral prefrontal cortex (VLPFC). The VLPFC is

815   involved in a host of functions related to active maintenance of stimulus information,

816   including being both a control and integrative node in the brain and an interface between

817   sensory and motor areas[42,43]. Not only does it handle awareness of the immediate

818   moment but also implementation of reactions to it. Furthermore, it is involved in forming

819   immediate connections between sensory processing and action control[42]. In addition, F7

820   integrates interoceptive, limbic emotion-motivational (from orbitofrontal and subcortical

821   areas), and sensory input (object identity from the ventral visual pathway) [42,44-46]. In

822   particular, visual information of behavioural significance travels from the ventral pathway to

823   the VLPFC, and later to the dorsolateral prefrontal cortex (DLPFC) and arcuate area. From

824   here additional information from the dorsal pathway is then integrated to form a precursor of

825   motor command[43]. In a transcranial magnetic stimulation (TMS) study, it was found that

826   the left VLPFC had a role in the regulation of negative emotions using positive reappraisal,

827   which is the ability to reinterpret the meaning of an emotional event or stimulus into a more

828   positive light. The VLPFC further produces a top-down biasing effect[47] that drives

829   selection and retrieval dynamics in the posterior cortex[42]. There also exists underlying

830   asymmetry in the activation of the IFG/AI. F7 refers to the left IFG, and it has been found

831   that incongruency in a flanker task activates IFG/AI, whereas the right IFG/AI (F8 was also a

832   top 5 feature along with F7 in the best time segment) is activated more by errors [48]. The

833   IFG/AI is also involved in post error slowing, where performance is slowed down due to

834   making an error[42]. The IFG/AI-anterior cingulate cortex network is also thought to be

835   involved in incongruency detection and resolving, and the ability to inhibit inappropriate

836   responses[42]. All together, it is not too far a stretch to imagine that a brain area involved in

837   immediate recognition, regulation, resolution and action on the incongruency and error in the

838   environment could be one of the key role players in susceptibility to cybersickness, and this

839   is reflected in its superior performance for prediction amongst all other features. The

840   additional discovery of F7 in part 2 of the analysis has led to a comprehensive picture of

841   cybersickness, in which there is now a node specific in function for integration and control in

842   response to incongruent environmental information commonly found in VR stimuli that

843   induce cybersickness[49] , in addition to areas mention above involved with visual

844   processing (O2) and motor planning (Cz).

845

846   *ECG*

847   This study tried to use ultra-short-term RMSSD recordings in an attempt to classify

848   cybersickness without having to capture more than 10 seconds of ECG data. Ultra-short-term

849   RMSSD recordings (30s and 10s) have been statistically reliable in previous studies, but this

850   parameter alone does not yield high accuracies (Table 4 and 5). Although reductions in

851   RMSSD have been associated with cybersickness intensity, more evidence is needed to explore

852   the role of parasympathetic cardiac indicators in cybersickness[50]. Conversely, nausea and

853   visually induced motion sickness have been found to be mediated by the brain with links to

854   sympathetic cardiac responses [28,51-53,34]. Although statistical differences between HRV

855   parameters were not found, it was found that classification algorithms for cybersickness using

856   sympathetic HRV indexes are still viable. This finding is shared with other studies where HRV

857   has shown promise for cybersickness classification[4]. This suggests that the differences in

858   sympathetic parameters of HRV in cybersick people versus control are more complex and

859   simpler types of statistical analysis may not pick up on it.

860

861   Future suggestions and limitations:

862   Given that HRV is computed using R-R intervals of an ECG wave, it may be the case that

863   other parameters, arising also from other aspects of the ECG wave could be helpful as

864   features, such as those used in detecting other pathologies like atrial fibrillation [54-56].

865   Further research could elucidate on this matter.

866

867   The NeuCube SNNr has some similarities to a liquid state machine (LSM)[57]. In a LSM,

868   both reservoir computing[58] and a spiking neural network is used to learn dynamical

869   systems. Spike inputs cause a propagation of spike activity throughout the reservoir, which

870   are like 'ripples' caused by a 'stone falling into liquid'. However, NeuCube differs in that the

871   structure is brain-inspired with stationary spatial mapping of inputs, and in that it uses

872   unsupervised and supervised learning[59]. This application of SNNr allowed for new

873   knowledge generation about CS and directed feature selection, and even revealed promising

874   targets for intervention. Still, the reservoir and output layer connections were detrimental to

875   classification performance. It is likely that these connections served as noise to the classified

876   feature vector. However, the information synthesized and stored within the SNNr is still

877   meaningful and valuable. Other training parameters of the cube could be optimized such as

878   the leak rate in membrane potential, the learning rate, refractory time for neuron firing and

879   number of training iterations[6]. Nonetheless this points towards the need for future research

880   on how to maximize interpretability and knowledge discovery alongside classification

881   performance. Moreover, given that SNNr activity is primarily influenced by its initial

882   connections, a careful consideration on how to initialize neurons within the SNNr is needed.

883   In this study the neurons within the SNNr have no distant connections because of the limited

884   radius set by the small world connectivity approach. However, in an actual brain, there are

885   both distant and local connections between neurons[60]. NeuCube allows for long distance

886   connections to be created through a probability [6], but these connections are not currently

887   biologically informed. Future research can expand on how to generate a more biologically

888   plausible SNNr and on how to use the information generated within it to enhance model

889   performance.

890

891   Some additional points also require consideration. This study used machine learning to

892   extract information about the spatiotemporal processes within the cybersick brain but future

893   studies could explore the role of the interplay between motor control, motor planning and

894   visual processing in VR on CS. The feature interaction network analysis only showed

895   interactions between cortical areas, but not whether they were increasing or decreasing

896   connections. Future studies could shed light on how key cybersickness centers in the brain act

897   to control the flow of information between cortical areas. Furthermore, the finding that

898   different features can be found at different time segments, but still give similar accuracies,

899   points towards the complexity of the cybersickness condition within the brain. It may

900   therefore be of interest to look at the change in features over time, rather than the features at

901   snapshots in time to understand cybersickness in more detail. Finally, it is not yet known if

902   the multimodal data fusion shown in this study could be improved by other biosignals and

903   this could be valuable research to conduct moving forwards.

904

905   Conclusion:

906   The paper proposes and demonstrates that a brain-inspired spiking neural network (SNN)

907   model can be created and used for on-the-spot prediction of cybersickness at resting state

908   baseline and near-instant detection of cybersickness during its onset. Using this SNN model

909   means that instead of storing raw data, each sample can be stored as a feature vector

910   representing brain activity, which means less memory storage and processing requirements.

911   The model can be dynamically updated on new data, modifying both the weighted template

912   neural map and the feature vectors to produce new insights. HRV alone or data fusion with

913   EEG are useful biosignals for the prediction and detection. Motor processing areas under Cz

914   and visual processing areas at O2 are key sites containing biomarkers as a precursor and

915   detector of cybersickness and could be useful target areas for clinical intervention.

916

917   **List of abbreviations**

918   VR – Virtual reality

919   CS – Cybersickness

920   ECG – Electrocardiogram

921   EEG – Electroencephalogram

922   SNN – Spiking neural network

923   HRV – Heart rate variability

924   KNN – K-nearest neighbor

925   LL – Left leg

926   RL – Right leg

927   LA – Left arm

928   RA – Right arm

929   MSSQ – Motion sickness susceptibility questionnaire

930   SSQ – Simulator sickness questionnaire

931   PNS – Parasympathetic nervous system index

932   SNS – Sympathetic nervous system index

933   SI – Stress index

934   SDNN – Standard deviation of N-N intervals

935   RMSSD – Root mean squared of successive differences

936   STDP – Spike timing dependent plasticity

937 SDSP – Spike driven synaptic plasticity

938 deSNN – Dynamic evolving spiking neural network

939 SF – Step forward

940 LSM – Liquid State Machine

941 SNNr – Spiking neural network reservoir

942 FIN – Feature interaction network

943 RO – Rank-order learning rule

944 LOOCV – Leave-one-out cross validation

945 SNR – Signal to noise ratio

946 LDA – Linear discriminant analysis

947 LightGBM – Light gradient boosting machine

948 GBDT – Gradient boosting decision tree

949 Goss – Gradient-based one-side sampling

950 Dart – dropouts meet multiple additive regression trees

951 VIMS – Visually induced motion sickness

952 VLPFC – Ventrolateral prefrontal cortex

953 DLPFC – Dorsolateral prefrontal cortex

954

962   **Code availability**: N/A

963   **Ethics approval**: N/A

964   **Consent for publication**: Consent from the authors of this review has been given for

965   publication.

966

967

968

969   **References**

970   1. Ball C, Huang K-T, Francis J (2021) Virtual reality adoption during the COVID-19 pandemic:
971   A uses and gratifications perspective. Telematics and Informatics 65:101728.
972   doi:https://doi.org/10.1016/j.tele.2021.101728
973   2. Cipresso P, Giglioli IAC, Raya MA, Riva G (2018) The Past, Present, and Future of Virtual
974   and Augmented Reality Research: A Network and Cluster Analysis of the Literature. Front
975   Psychol 9:2086. doi:10.3389/fpsyg.2018.02086
976   3. Rebenitsch L, Owen C (2016) Review on cybersickness in applications and visual displays.
977   Virtual Reality 20 (2):101-125. doi:10.1007/s10055-016-0285-9
978   4. Yang AHX, Kasabov N, Cakmak YO (2022) Machine learning methods for the study of
979   cybersickness: a systematic review. Brain Informatics 9 (1):24. doi:10.1186/s40708-022-
980   00172-6
981   5. Kundu RK, Islam R, Quarles J, Hoque KA (2023) LiteVR: Interpretable and Lightweight
982   Cybersickness Detection using Explainable AI. arXiv preprint arXiv:230203037
983   6. Kasabov NK (2014) NeuCube: A spiking neural network architecture for mapping, learning
984   and understanding of spatio-temporal brain data. Neural networks 52:62-76.
985   doi:10.1016/j.neunet.2014.01.006
986   7. Kasabov NK (2018) Time-Space, Spiking Neural Networks and Brain-Inspired Artificial
987   Intelligence (Springer Series on Bio- and Neurosystems). Springer Publishing Company,
988   Incorporated,
989   8. Kasabov NK (2007) Evolving connectionist systems: the knowledge engineering approach.
990   Springer Science & Business Media,
991   9. Bohte SM (2004) The evidence for neural information processing with precise spike-
992   times: A survey. Natural Computing 3 (2):195-206.
993   doi:10.1023/B:NACO.0000027755.02868.60
994   10. Kasabov N (2010) To spike or not to spike: a probabilistic spiking neuron model. Neural
995   Netw 23 (1):16-19. doi:10.1016/j.neunet.2009.08.010
996   11. Kasabov N, Dhoble K, Nuntalid N, Indiveri G (2013) Dynamic evolving spiking neural
997   networks for on-line spatio- and spectro-temporal pattern recognition. Neural Netw 41:188-
998   201. doi:10.1016/j.neunet.2012.11.014
999   12. Mohemmed A, Schliebs S, Matsuda S, Kasabov N (2012) Span: Spike pattern association
1000 neuron for learning spatio-temporal spike patterns. International journal of neural systems
1001 22 (04):1250012

13. Demertzis K, Iliadis L, Bougoudis I (2020) Gryphon: a semi-supervised anomaly detection system based on one-class evolving spiking neural network. Neural Computing and Applications 32. doi:10.1007/s00521-019-04363-x

14. Tarvainen MP, Niskanen JP, Lipponen JA, Ranta-aho PO, Karjalainen PA (2014) Kubios HRV - heart rate variability analysis software. Computer Methods and Programs in Biomedicine 113 (1):210-220. doi:10.1016/j.cmpb.2013.07.024

15. Makowski D, Pham T, Lau ZJ, Brammer JC, Lespinasse F, Pham H, Schölzel C, Chen SHA (2021) NeuroKit2: A Python toolbox for neurophysiological signal processing. Behav Res Methods 53 (4):1689-1696. doi:10.3758/s13428-020-01516-y

16. Gomes P, Margaritoff P, Silva H pyHRV: Development and evaluation of an open-source python toolbox for heart rate variability (HRV). In: Proc. Int'l conf. On electrical, electronic and computing engineering (icetran), 2019. pp 822-828

17. Padmanaban N, Ruban T, Sitzmann V, Norcia A, Wetzstein G (2018) Towards a Machine-Learning Approach for Sickness Prediction in 360° Stereoscopic Videos. IEEE Transactions on Visualization and Computer Graphics PP:1-1. doi:10.1109/TVCG.2018.2793560

18. Golding JF (2006) Predicting individual differences in motion sickness susceptibility by questionnaire. Personality and Individual Differences 41 (2):237-248. doi:10.1016/J.PAID.2006.01.012

19. Kennedy RS, Lane NE, Berbaum KS, Lilienthal MG (1993) Simulator Sickness Questionnaire: An Enhanced Method for Quantifying Simulator Sickness. The International Journal of Aviation Psychology 3 (3):203-220. doi:10.1207/s15327108ijap0303_3

20. Kasabov N, Scott N, Tu E, Marks S, Sengupta N, Capecci E, Othman M, Doborjeh M, Murli N, Hartono R (2016) Design methodology and selected applications of evolving spatio-temporal data machines in the NeuCube neuromorphic framework. Neural Networks 78 (2016)):1-14

21. Yoneyama M, Fukushima Y, Tsukada M, Aihara T (2011) Spatiotemporal characteristics of synaptic EPSP summation on the dendritic trees of hippocampal CA1 pyramidal neurons as revealed by laser uncaging stimulation. Cogn Neurodyn 5 (4):333-342. doi:10.1007/s11571-011-9158-9

22. Giuliodori MJ, Zuccolilli G (2004) POSTSYNAPTIC POTENTIAL SUMMATION AND ACTION POTENTIAL INITIATION: FUNCTION FOLLOWING FORM. Advances in Physiology Education 28 (2):79-80. doi:10.1152/advan.00051.2003

23. Bear MF, Malenka RC (1994) Synaptic plasticity: LTP and LTD. Curr Opin Neurobiol 4 (3):389-399. doi:10.1016/0959-4388(94)90101-5

24. Tan C, Šarlija M, Kasabov N (2020) Spiking Neural Networks: Background, Recent Development and the NeuCube Architecture. Neural Processing Letters 52 (2):1675-1701. doi:10.1007/s11063-020-10322-8

25. Shaffer F, Ginsberg JP (2017) An Overview of Heart Rate Variability Metrics and Norms. Frontiers in Public Health 5 (September):1-17. doi:10.3389/fpubh.2017.00258

26. Lee Y, Alamaniotis M (2020) Unsupervised EEG Cybersickness Prediction with Deep Embedded Self Organizing Map. 2020 IEEE 20th International Conference on Bioinformatics and Bioengineering (BIBE):538-542. doi:10.1109/BIBE50027.2020.00093

27. Nam YH, Kim YY, Kim HT, Ko HD, Park KS (2001) Automatic detection of nausea using bio-signals during immersion in a virtual reality environment. 2001 Conference Proceedings of the 23rd Annual International Conference of the IEEE Engineering in Medicine and Biology Society 2:2013-2015 vol.2012. doi:10.1109/IEMBS.2001.1020626

1048 28. Farmer AD, Ban VF, Coen SJ, Sanger GJ, Barker GJ, Gresty MA, Giampietro VP, Williams
1049 SC, Webb DL, Hellström PM, Andrews PL, Aziz Q (2015) Visually induced nausea causes
1050 characteristic changes in cerebral, autonomic and endocrine function in humans. J Physiol
1051 593 (5):1183-1196. doi:10.1113/jphysiol.2014.284240
1052 29. Golding JF, Rafiq A, Keshavarz B (2021) Predicting Individual Susceptibility to Visually
1053 Induced Motion Sickness by Questionnaire. Frontiers in Virtual Reality 2 (3).
1054 doi:10.3389/frvir.2021.576871
1055 30. Liu R, Xu M, Zhang Y, Peli E, Hwang AD (2020) A Pilot Study on Electroencephalogram-
1056 based Evaluation of Visually Induced Motion Sickness. Journal of Imaging Science and
1057 Technology 64 (2):20501-20501-20501-20510.
1058 doi:10.2352/J.ImagingSci.Technol.2020.64.2.020501
1059 31. Miyazaki J, Yamamoto H, Ichimura Y, Yamashiro H, Murase T, Yamamoto T, Umeda M,
1060 Higuchi T (2021) Resting-state functional connectivity predicts recovery from visually
1061 induced motion sickness. Experimental Brain Research. doi:10.1007/s00221-020-06002-7
1062 32. Li Y, Liu A, Ding L (2019) Machine learning assessment of visually induced motion
1063 sickness levels based on multiple biosignals. Biomedical Signal Processing and Control
1064 49:202-211. doi:10.1016/j.bspc.2018.12.007
1065 33. Khoirunnisaa AZ, Pane ES, Wibawa AD, Purnomo MH (2018) Channel Selection of EEG-
1066 Based Cybersickness Recognition during Playing Video Game Using Correlation Feature
1067 Selection (CFS). 2018 2nd International Conference on Biomedical Engineering
1068 (IBIOMED):48-53. doi:10.1109/IBIOMED.2018.8534877
1069 34. Toschi N, Kim J, Sclocco R, Duggento A, Barbieri R, Kuo B, Napadow V (2017) Motion
1070 sickness increases functional connectivity between visual motion and nausea-associated
1071 brain regions. Auton Neurosci 202:108-113. doi:10.1016/j.autneu.2016.10.003
1072 10.1016/j.autneu.2016.10.003. Epub 2016 Oct 17.
1073 35. Krokos E, Varshney A (2021) Quantifying VR cybersickness using EEG. Virtual Reality.
1074 doi:10.1007/s10055-021-00517-2
1075 36. Tard C, Delval A, Devos D, Lopes R, Lenfant P, Dujardin K, Hossein-Foucher C, Semah F,
1076 Duhamel A, Defebvre L, Le Jeune F, Moreau C (2015) Brain metabolic abnormalities during
1077 gait with freezing in Parkinson's disease. Neuroscience 307:281-301.
1078 doi:10.1016/j.neuroscience.2015.08.063
1079 37. Mackenzie TN, Bailey AZ, Mi PY, Tsang P, Jones CB, Nelson AJ (2016) Human area 5
1080 modulates corticospinal output during movement preparation. NeuroReport 27 (14):1056-
1081 1060. doi:10.1097/wnr.0000000000000655
1082 38. Palmisano S, Arcioni B, Stapley PJ (2018) Predicting vection and visually induced motion
1083 sickness based on spontaneous postural activity. Exp Brain Res 236 (1):315-329.
1084 doi:10.1007/s00221-017-5130-1
1085 39. Campana G, Cowey A, Walsh V (2006) Visual Area V5/MT Remembers "What" but Not
1086 "Where". Cerebral Cortex 16 (12):1766-1770. doi:10.1093/cercor/bhj111
1087 40. Farmer AD, Ban VF, Coen SJ, Sanger GJ, Barker GJ, Gresty MA, Giampietro VP, Williams
1088 SC, Webb DL, Hellström PM, Andrews PLR, Aziz Q (2015) Visually induced nausea causes
1089 characteristic changes in cerebral, autonomic and endocrine function in humans. The
1090 Journal of physiology 593 (5):1183-1196. doi:10.1113/jphysiol.2014.284240
1091 41. Scrivener CL, Reader AT (2022) Variability of EEG electrode positions and their
1092 underlying brain regions: visualizing gel artifacts from a simultaneous EEG-fMRI dataset.
1093 Brain Behav 12 (2):e2476. doi:10.1002/brb3.2476

1094   42. Tops M, Boksem MA (2011) A potential role of the inferior frontal gyrus and anterior
1095   insula in cognitive control, brain rhythms, and event-related potentials. Front Psychol 2:330.
1096   doi:10.3389/fpsyg.2011.00330
1097   43. Sakagami M, Pan X (2007) Functional role of the ventrolateral prefrontal cortex in
1098   decision making. Curr Opin Neurobiol 17 (2):228-233. doi:10.1016/j.conb.2007.02.008
1099   44. Craig A (2008) Handbook of emotions. Interoception and emotion a neuroanatomical
1100   perspective. Guilford Press,
1101   45. Craig AD (2002) How do you feel? Interoception: the sense of the physiological condition
1102   of the body. Nat Rev Neurosci 3 (8):655-666. doi:10.1038/nrn894
1103   10.1038/nrn894.
1104   46. Craig AD (2009) How do you feel — now? The anterior insula and human awareness.
1105   Nature Reviews Neuroscience 10 (1):59-70. doi:10.1038/nrn2555
1106   47. Beck DM, Kastner S (2009) Top-down and bottom-up mechanisms in biasing competition
1107   in the human brain. Vision Res 49 (10):1154-1165. doi:10.1016/j.visres.2008.07.012
1108   48. Ullsperger M, Harsay HA, Wessel JR, Ridderinkhof KR (2010) Conscious perception of
1109   errors and its relation to the anterior insula. Brain Structure and Function 214:629-643
1110   49. Porcino T, Trevisan D, Clua E (2020) Minimizing cybersickness in head-mounted display
1111   systems: causes and strategies review. doi:10.1109/SVR51698.2020.00035
1112   50. Mazloumi Gavgani A, Hodgson DM, Nalivaiko E (2017) Effects of visual flow direction on
1113   signs and symptoms of cybersickness. PloS one 12 (8):e0182790-e0182790.
1114   doi:10.1371/journal.pone.0182790
1115   51. Holmes SR, Griffin MJ (2001) Correlation between heart rate and the severity of motion
1116   sickness caused by optokinetic stimulation. Journal of Psychophysiology 15 (1):35-42.
1117   doi:10.1027//0269-8803.15.1.35
1118   52. Ruffle JK, Patel A, Giampietro V, Howard MA, Sanger GJ, Andrews PLR, Williams SCR, Aziz
1119   Q, Farmer AD (2019) Functional brain networks and neuroanatomy underpinning nausea
1120   severity can predict nausea susceptibility using machine learning. The Journal of Physiology
1121   597 (6):1517-1529. doi:https://doi.org/10.1113/JP277474
1122   53. Sclocco R, Kim J, Garcia RG, Sheehan JD, Beissner F, Bianchi AM, Cerutti S, Kuo B,
1123   Barbieri R, Napadow V (2016) Brain Circuitry Supporting Multi-Organ Autonomic Outflow in
1124   Response to Nausea. Cereb Cortex 26 (2):485-497. doi:10.1093/cercor/bhu172
1125   10.1093/cercor/bhu172. Epub 2014 Aug 12.
1126   54. Maršánová L, Ronzhina M, Smíšek R, Vítek M, Němcová A, Smital L, Nováková M (2017)
1127   ECG features and methods for automatic classification of ventricular premature and
1128   ischemic heartbeats: A comprehensive experimental study. Scientific Reports 7 (1):11239.
1129   doi:10.1038/s41598-017-10942-6
1130   55. Doquire G, de Lannoy G, François D, Verleysen M (2011) Feature selection for
1131   interpatient supervised heart beat classification. Comput Intell Neurosci 2011:643816.
1132   doi:10.1155/2011/643816
1133   56. Rizwan A, Zoha A, Mabrouk IB, Sabbour HM, Al-Sumaiti AS, Alomainy A, Imran MA,
1134   Abbasi QH (2021) A Review on the State of the Art in Atrial Fibrillation Detection Enabled by
1135   Machine Learning. IEEE Reviews in Biomedical Engineering 14:219-239.
1136   doi:10.1109/RBME.2020.2976507
1137   57. Maass W (2011) Liquid State Machines: Motivation, Theory, and Applications. In:
1138   Computability in Context. IMPERIAL COLLEGE PRESS, pp 275-296.
1139   doi:doi:10.1142/9781848162778_0008
1140   10.1142/9781848162778_0008

1141   58. Gauthier DJ, Bollt E, Griffith A, Barbosa WAS (2021) Next generation reservoir
1142   computing. Nature Communications 12 (1):5564. doi:10.1038/s41467-021-25801-2
1143   59. Behrenbeck J, Tayeb Z, Bhiri C, Richter C, Rhodes O, Kasabov N, Espinosa-Ramos JI,
1144   Furber S, Cheng G, Conradt J (2019) Classification and regression of spatio-temporal signals
1145   using NeuCube and its realization on SpiNNaker neuromorphic hardware. J Neural Eng 16
1146   (2):026014
1147   60. Chanraud S, Zahr N, Sullivan EV, Pfefferbaum A (2010) MR diffusion tensor imaging: a
1148   window into white matter integrity of the working brain. Neuropsychol Rev 20 (2):209-225.
1149   doi:10.1007/s11065-010-9129-7

1150

1151